energies

MDPI

Article

Electromagnetic Vibration and Noise Analysis of Linear Phase-Shifting Transformer

Dongao Yan, Jinghong Zhao, Sinian Yan *, Hanming Wang and Changduo Zhou

School of Electrical Engineering, Naval University of Engineering, Wuhan 430033, China
* Correspondence: ysnian0504@126.com

Abstract: The advantages of adjustable angle phase-shifting and great expansibility make the linear phase-shifting transformer a novel type of power conversion device with a wide range of potential applications. However, during the procedure, there is a lot of noise. For the purposes of transformer design and vibration and noise reduction, it is crucial to investigate its electromagnetic vibration and noise. In this paper, the radial electromagnetic force wave considering the influence of the end effect as the source of the noise of the linear phase-shifting transformer was deduced and calculated. Based on this, the spectrum and space–time properties of the radial electromagnetic force waves were simulated and verified. Additionally, a finite element model was created using the Ansys Workbench 2022R1 platform to study the electromagnetic vibration and noise of the linear phase-shifting transformer. A joint simulation of the electromagnetic, structural, and sound fields was then performed. First, the transformer's natural frequency was determined by modal analysis. After that, the transformer's structure and the results of the transient electromagnetic field computation were combined and a harmonic response analysis was conducted to determine the vibration acceleration spectrum. Finally, in order to solve the sound pressure field, the transformer's boundary vibration acceleration was coupled to the air domain. Furthermore, an analysis was conducted to determine the noise distribution surrounding the linear phase-shifting transformer. The joint simulation findings demonstrate that the linear phase-shifting transformer's resonance, which produces larger electromagnetic vibration and noise, is indeed caused by the radial electromagnetic force. Simultaneously, the impact of the LPST core's fixed components on the electromagnetic vibration and noise of the core was examined.

Keywords: linear phase-shifting transformer; radial electromagnetic force; finite element method; electromagnetic vibration noise

check for updates

Citation: Yan, D.; Zhao, J.; Yan, S.; Wang, H.; Zhou, C. Electromagnetic Vibration and Noise Analysis of Linear Phase-Shifting Transformer. *Energies* **2024**, *17*, 1448. https://doi.org/10.3390/en17061448

Academic Editor: Andrea Mariscotti

Received: 17 February 2024
Revised: 12 March 2024
Accepted: 12 March 2024
Published: 17 March 2024

Copyright: © 2024 by the authors. Licensee MDPI, Basel, Switzerland. This article is an open access article distributed under the terms and conditions of the Creative Commons Attribution (CC BY) license (https://creativecommons.org/licenses/by/4.0/).

1. Introduction

As an important carrier for the realization of multiple superimposed inverter technology, phase-shifting transformers are mainly divided into three types: core type, circular type, and linear type. Compared with the first two types of phase-shifting transformers, the linear phase-shifting transformer (LPST) can not only realize the functions of phase-shifting and superposition, but also has the advantages of arbitrary angle phase-shifting, good expansibility, and easy modularization [1].

However, the vibration and noise during the LPST's operation are problems that cannot be ignored. Vibration is the cause of noise. The vibration of the LPST will produce displacement, which will compress and sparse the surrounding air or medium. These changes are transmitted in the form of waves at the speed of sound to form sound. This not only affects the surrounding environment, but also reduces the service life of the equipment [2,3]. The electromagnetic vibration of the LPST is determined by the electromagnetic force and the natural frequency of the structure [4]. When the low-order natural frequency of the structural system is close to the frequency of the electromagnetic force and is in the frequency range that can cause resonance, the transformer structure will produce large-scale

vibration, which in turn produces large noise. The noise can even reach a level of more than 80 dBA. Therefore, when analyzing the vibration generated by the electromagnetic force of the LPST, it is necessary to pay attention to the low-order natural vibration frequency of the structural system to observe whether there is resonance phenomena so as to avoid the occurrence of resonance phenomena in the design stage [5].

The structure and principle of the LPST are similar to those of linear motors. Thus, a lot can be learned about its electromagnetic vibration and noise from the experience of working with traditional motors and transformers. The research on the electromagnetic vibration of transformers began in the early 20th century. The main research object is the magnetostrictive effect of the iron core, for which the main research methods are the experimental method, numerical method, and analytical method [6]. Starting from the mechanism of transformer noise generation, the finite element model of the oil-immersed power three-column double-winding transformer is established in Ref. [7]. However, this paper only considers the influence of the magnetostrictive force and does not consider the influence of the electromagnetic force. The electromagnetic field and structural force field are coupled and calculated, and the vibrations of the transformer core and winding are obtained. However, the structure of the LPST is different from the traditional transformer and it will be affected by the radial electromagnetic force. Scholars in Zhejiang University have carried out comparative analyses and experimental research on the electromagnetic vibration of permanent magnet synchronous motors. The radial electromagnetic force calculated by finite element simulation of the two-dimensional electromagnetic field is directly coupled to the transient structural finite element model of the motor, and the vibration of the permanent magnet synchronous motor can be calculated [8]. Ref. [9] analyzed the vibration of the permanent magnet linear synchronous motor core when considering both the radial electromagnetic force and magnetostrictive force. The acoustic-solid coupling simulation analysis was carried out by the finite element software COMSOL Multiphysics 6.0. Ref. [10] studied and analyzed the vibration and noise reduction of the switched reluctance motor, and concluded that the radial electromagnetic force wave is the main source of motor vibration. However, the analytical expression of the radial electromagnetic force was not derived. Ref. [11] studied the frequency conversion motor and explored the influence of frequency conversion harmonics on the noise characteristics of the motor. It was concluded that the output harmonic of the frequency converter will make the frequency conversion motor emit noise of various frequencies, which makes the motor more prone to resonance, and that this needs to be eliminated or weakened at the design stage. Based on the electromagnetic force of the air gap of the motor, the spatial order and frequency characteristics of the electromagnetic force and its influence on the electromagnetic vibration are analyzed in Ref. [12]. In Ref. [13], the modal analysis and calculation of the linear motor were carried out, and it was concluded that the electromagnetic force generated during the speed regulation of the motor under no-load conditions could easily lead to resonance of the motor. However, the influence of the edge effect was not considered. Based on the research status at home and abroad [6,14–19], at this stage, scholars in various countries have focused on the study of electromagnetic vibration in rotating motors, and there are relatively few studies on the vibration and noise of linear motors and the LPST. One of the important research points is the influence of the end effect on the air gap electromagnetic force.

In this paper, the principle of vibration and noise of the LPST are analyzed theoretically. The radial electromagnetic force wave considering the influence of the end effect is deduced and calculated. The LPST simulation model is established by the finite element analysis software ANSYS Maxwell 2022R1 and Workbench 2022R1. The electromagnetic field analysis, modal analysis, harmonic response analysis, and noise analysis of the model are carried out, respectively. The distribution characteristics of vibration and noise during LPST operation are obtained, which provide theoretical support for vibration and noise reduction in the early design stage.

2. Structure and Operating Principle of Linear Phase-Shifting Transformer

As a new type of power conversion equipment, the basic principle of the LPST is similar to that of a linear induction motor. The structure (as shown in Figure 1) is approximately equivalent to a linear induction motor with a slip rate of 1. In this paper, a double-layer laminated winding LPST for a multiple superimposed inverter system is selected for analysis. The specific parameters are shown in Table 1, and the schematic diagram of the transformer winding structure is shown in Figure 2.

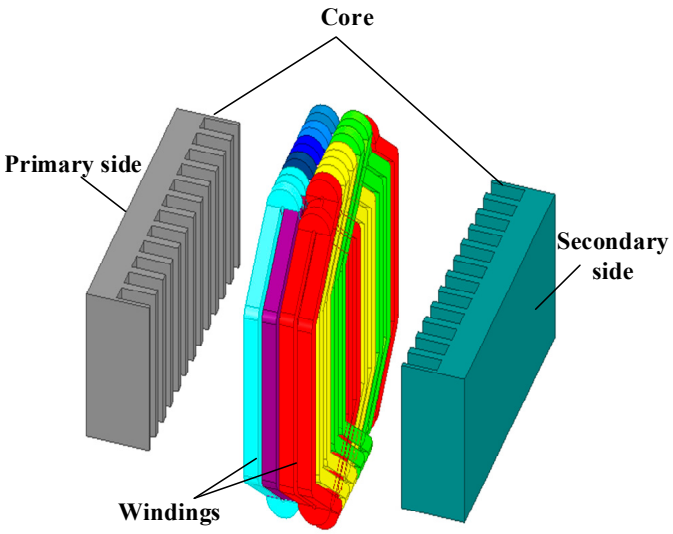


Figure 1. Three-dimensional structure diagram of LPST model.

Table 1. Main structural parameters of LPST.

Symbol	Meaning	Value	Unit
Q	Slot number	12	-
N_1	Number of primary side windings	300	-
N_2	Number of secondary side windings	240	-
L_m	Core length	210	mm
L_b	Core stack thickness	90	mm
L_h	Core height	40	mm
δ	Air gap length	0.3	mm
b_0	Slot width	12	mm
b_τ	Tooth pitch	17.5	mm
p	Number of pole pairs	1	-
τ	Polar distance	105	mm

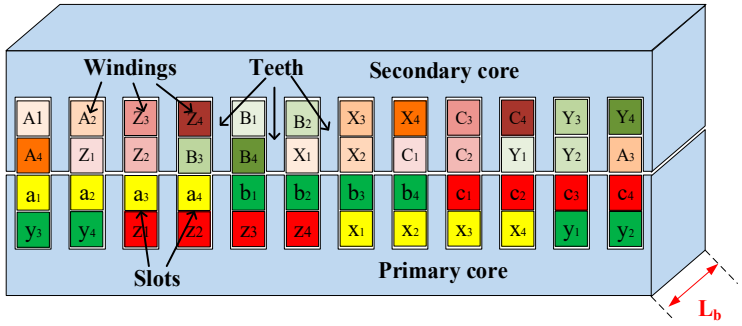


Figure 2. LPST winding structure diagram.

The primary side of the LPST has 12-phase windings (a1–x1, a2–x2, a3–x3, a4–x4, b1–y1, b2–y2, b3–y3, b4–y4, c1–z1, c2–z2, c3–z3, c4–z4) and adopts a double-layer winding structure. The pitch y_{11} is τ. The connection modes of the windings are star-shaped, and their neutral points are O1, O2, O3, and O4, respectively. Figure 3 is the expansion diagram of the primary side windings. There are three-phase windings (A–X, B–Y, C–Z) on the secondary side of the LPST, and the double-layer winding structure is also adopted. The connection mode of windings A, B, and C is star-shaped, and the neutral point is O. The three-phase winding of the secondary side is a combination of short-pitch windings and long-pitch windings. The long pitch y_{13} is $7\tau/6$ and the short pitch y_{12} is $5\tau/6$. Figure 4 is the expansion diagram of the primary side windings.

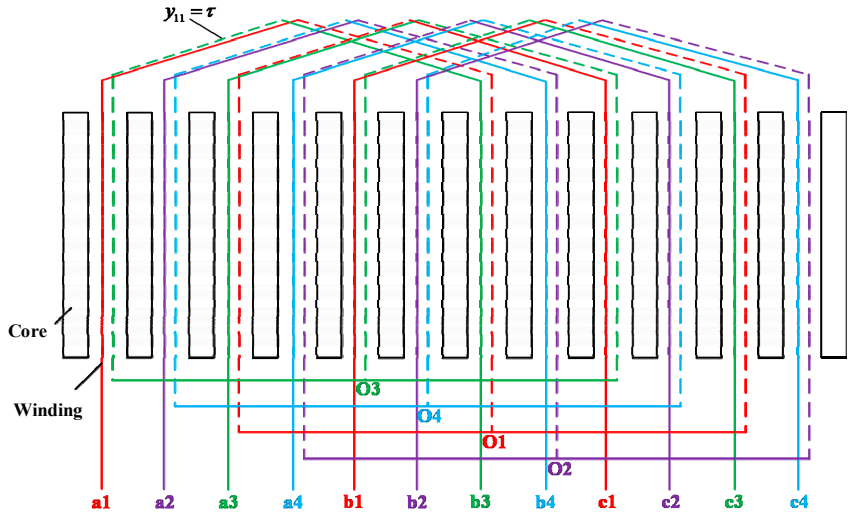


Figure 3. LPST expansion diagram of the primary side windings.

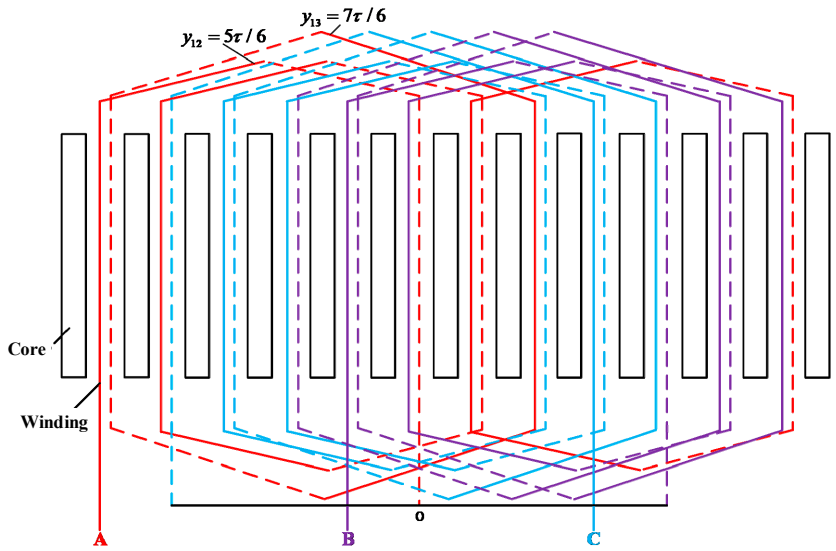


Figure 4. LPST expansion diagram of the secondary side windings.

When the LPST is applied to the multi-superposition inverter system, twelve groups of windings are embedded in the primary side, four groups of three-phase bridge inverter circuits are connected in parallel, and four groups of three-phase windings are formed by a star connection. Twelve sets of windings are embedded in the secondary side, and then the star connection is connected in series to form a three-phase winding, which leads to three connection terminals and accesses to the load. The detailed structure of the system is shown in Figure 5. The operating condition information is shown in Table 2.

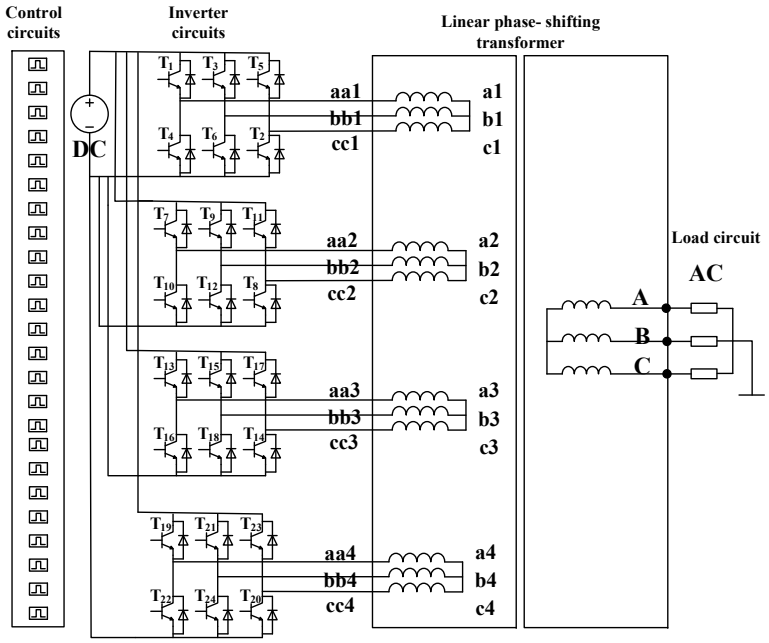


Figure 5. Structure diagram of LPST multi-stack inverter system.

Table 2. Operating condition of LPST.

Parameters	Value	Unit	Remark
DC bus voltage	130	V	-
Switching frequency	50	Hz	-
Rated power	0.8	kVA	-
Load	0	Ω	No-load condition
	50	Ω	Load condition

3. Radial Electromagnetic Force Calculation

To facilitate the analysis, the following assumptions need to be made:

(1) Ignore the impact of core saturation;
(2) The permeability of the iron core is regarded as infinity;
(3) It is considered that the air gap magnetic field is constant in the thickness direction of the transformer.
(4) The Cartesian coordinate system and the direction of the radial electromagnetic force of the LPST are shown in Figure 6.

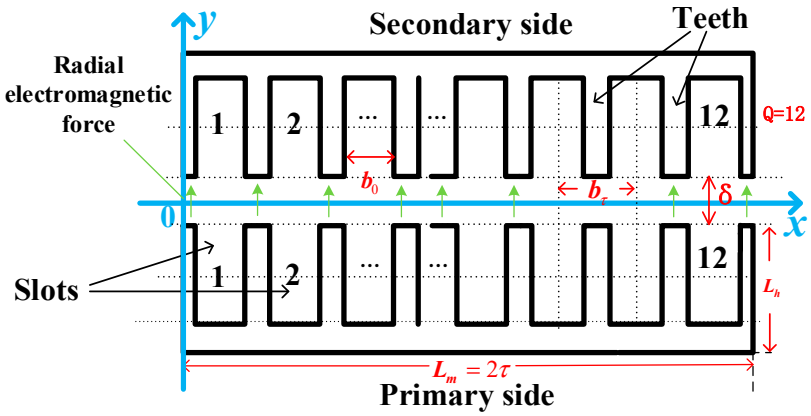


Figure 6. The schematic diagram of LPST coordinate system.

When the magnetic saturation of the core is neglected, the instantaneous value of the air gap flux density is expressed as

$$B(x,t) = f(x,t)\Lambda(x), \tag{1}$$

where $f(x,t)$ is the air gap magnetomotive force and $\Lambda(x)$ is the air gap permeance.

At the input port of the LPST, the phase voltage output of the three-phase inverter circuit is a 6-step wave. The four groups of 6-step waves lag 15 degrees in turn, and the superposition is synthesized into a 24-step wave, which approaches the sine wave, as shown in Figure 7.

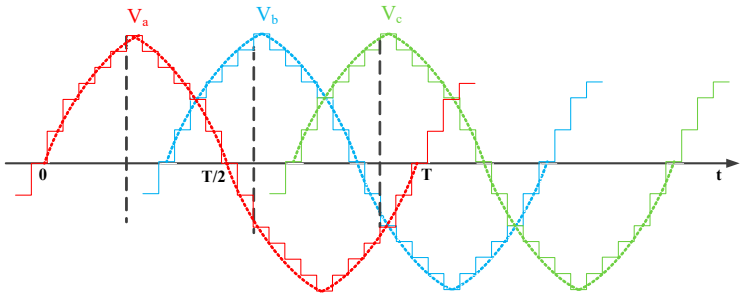


Figure 7. Diagram of 24-step wave.

According to the principle of phase shift superposition, the other harmonics are offset in the process of phase shift superposition. Only some harmonics of certain frequencies are left. It can be seen from Ref. [1] that the equivalent output voltage 24-step wave of the inverter in Fourier series form can be expressed as

$$\begin{cases} u_A = \sum\limits_{n=1,23,25,\cdots}^{\infty} \frac{4U_d}{n\pi} \sin(n\omega t) \\ u_B = \sum\limits_{n=1,23,25,\cdots}^{\infty} \frac{4U_d}{n\pi} \sin\left[n(\omega t - \frac{2\pi}{3})\right], \\ u_C = \sum\limits_{n=1,23,25,\cdots}^{\infty} \frac{4U_d}{n\pi} \sin\left[n(\omega t + \frac{2\pi}{3})\right] \end{cases} \tag{2}$$

where U_d is the DC bus voltage, $n = 1, 24m \pm 1 \cdots, m = 1, 2, 3 \cdots$ is the harmonic number, and ω is the angular frequency of the inverter power supply.

After the high-frequency harmonic voltage generated by the inverter circuit is injected into the primary side winding of the LPST, the harmonic current of the same frequency will inevitably be generated. According to the load formula $I = \frac{U}{Z}$ and the above voltage formula, the equivalent three-phase current $i_A(t)$, $i_B(t)$, $i_C(t)$ of the four groups of inverter circuit inputs into the winding can be expressed as

$$\begin{cases} i_A = \sum\limits_{n}^{\infty} I_n \sin(n\omega t) \\ i_B = \sum\limits_{n}^{\infty} I_n \sin\left[n(\omega t - \frac{2\pi}{3})\right], \\ i_C = \sum\limits_{n}^{\infty} I_n \sin\left[n(\omega t + \frac{2\pi}{3})\right] \end{cases} \tag{3}$$

where I_n is the amplitude of the nth harmonic current and $n = 1, 24m \pm 1 \cdots, m = 1, 2, 3 \cdots$.

According to the principle of winding magnetomotive force generation, the magnetomotive force of each phase is expressed as

$$\begin{cases} f_{A1} = F_{\phi 1}\cos\frac{\pi}{\tau}x\sum\limits_{n}^{\infty}\sin(n\omega t) \\ f_{B1} = F_{\phi 1}\cos\left(\frac{\pi}{\tau}x-\frac{2\pi}{3}\right)\sum\limits_{n}^{\infty}\sin\left[n\left(\omega t-\frac{2\pi}{3}\right)\right], \\ f_{C1} = F_{\phi 1}\cos\left(\frac{\pi}{\tau}x+\frac{2\pi}{3}\right)\sum\limits_{n}^{\infty}\sin\left[n\left(\omega t+\frac{2\pi}{3}\right)\right] \end{cases} \tag{4}$$

According to the product-to-sum formula, the following can be obtained by adding the pulsating magnetomotive forces of phase A, phase B, and phase C:

$$\begin{aligned} f_1(x,t) &= f_{A1}+f_{B1}+f_{C1} \\ &= \sum_{n}^{\infty}F_n\sin(n\omega t-\tfrac{\pi}{\tau}x), \end{aligned} \tag{5}$$

$$F_n = \frac{3}{2}F_{\phi 1} = 1.35\frac{N_1K_{w1}}{p}I_n, \tag{6}$$

Similarly, the synthetic magnetomotive force $f_v(x,t)$ can be obtained by adding the subharmonic magnetomotive force generated by the windings of phase A, B, and C, that is

$$\begin{aligned} f_v(x,t) &= f_{Av}+f_{Bv}+f_{Cv} \\ &= F_{\phi\nu}\cos\nu\tfrac{\pi}{\tau}x\sum_{n}^{\infty}\sin(n\omega t)+F_{\phi\nu}\cos\nu(\tfrac{\pi}{\tau}x-\tfrac{2\pi}{3})\sum_{n}^{\infty}\sin\left[n\left(\omega t-\tfrac{2\pi}{3}\right)\right] \\ &+F_{\phi\nu}\cos\nu(\tfrac{\pi}{\tau}x+\tfrac{2\pi}{3})\sum_{n}^{\infty}\sin\left[n\left(\omega t+\tfrac{2\pi}{3}\right)\right] \end{aligned}, \tag{7}$$

(1) When $\nu = 3k(k = 1,2,3\cdots)$

$$f_v(x,t) = 0, \tag{8}$$

(2) When $\nu = 6k+1(k = 1,2,3\cdots)$

$$f_v(x,t) = \frac{3}{2}F_{\phi\nu}\sum_{n}^{\infty}\sin\left(n\omega t-\nu\cdot\frac{\pi}{\tau}x\right), \tag{9}$$

(3) When $\nu = 6k-1(k = 1,2,3\cdots)$

$$f_v(x,t) = \frac{3}{2}F_{\phi\nu}\sum_{n}^{\infty}\sin\left(n\omega t+\nu\cdot\frac{\pi}{\tau}x\right), \tag{10}$$

Therefore, the total magnetomotive force of the primary side winding can be expressed as

$$\begin{aligned} f(x,t) &= f_1(x,t)+f_v(x,t) \\ &= \sum_{n=1,24m\pm1,\cdots}^{\infty}F_n\sin(n\omega t-\tfrac{\pi}{\tau}x)+\sum_{\nu=6k\pm1}^{\infty}\sum_{n}^{\infty}F_\nu\sin\left(n\omega t\pm\nu\cdot\tfrac{\pi}{\tau}x\right), \end{aligned} \tag{11}$$

In Formula (13)

$$F_\nu = \frac{3}{2}F_{\phi\nu} = 1.35\frac{N_1K_{w\nu}}{\nu p}I_n, \tag{12}$$

$$K_{w\nu} = \sin\left(\frac{\pi\nu y_{11}}{2p\tau}\right)\frac{\sin\left(q\frac{\nu\alpha}{2p}\right)}{q\sin\frac{\nu\alpha}{2p}}, \tag{13}$$

where $K_{w\nu}$ is the winding coefficient, which is 0.966 for primary windings; α is the slot pitch electric angle; and q is the slot number per pole and per phase.

For the LPST, there are several slots on the primary and secondary sides, and the permeance at different positions of the air gap is related to the corresponding magnetic flux path. The conformal transformation method is a method to calculate the equivalent slot for

an air gap magnetic field. According to Ref. [20], the air gap magnetic permeance of the LPST can be expressed as

$$\Lambda(x) = \Lambda_0 \lambda(x), \tag{14}$$

where $\Lambda_0 = {}^{\mu_0}\big/{}_{\delta K_c}$. $\lambda(x)$ is the relative permeability ratio and K_c is the Carter coefficient. In addition, K_c is expressed as

$$K_c = K_{c1} K_{c2}, \tag{15}$$

where K_{c1} is the Carter coefficient under the condition that the secondary side core is smooth and the primary side core is slotted and K_{c2} is the Carter coefficient under the condition that the secondary side core is slotted and the primary side core is smooth. Due to the symmetry of the LPST, they can be expressed as

$$K_{c1} = K_{c2} = \frac{b_\tau}{b_\tau - \gamma_1 \delta}, \tag{16}$$

where

$$\gamma_1 = \frac{4}{\pi}\left[\left(\frac{b_0}{2\delta}\right)\arctan\left(\frac{b_0}{2\delta}\right) - \ln\sqrt{1+\left(\frac{b_0}{2\delta}\right)^2}\right], \tag{17}$$

A coordinate system is established in a single slot, as shown in Figure 8. The relative permeability ratio in a single slot can be expressed as

$$\lambda(x) = \begin{cases} 1 & 0.4b_0 < x \le \frac{b_\tau}{2} \\ 1 - \beta - \beta\cos(\frac{\pi}{0.8b_0}x) & |x| \le 0.4b_0 \\ 1 & -\frac{b_\tau}{2} \le x < -0.4b_0 \end{cases}, \tag{18}$$

where

$$\begin{cases} aa = \frac{b_0}{2\delta} \\ aa' = aa + \sqrt{1+aa^2} \\ \beta = \frac{1+aa'^2-2aa'}{2+2aa'^2} \end{cases}, \tag{19}$$

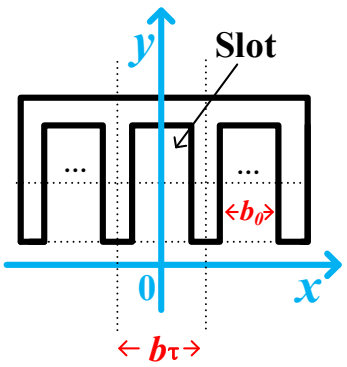


Figure 8. The coordinate system in a single slot.

Ignoring the influence of adjacent slots, Equation (18) is extended with the tooth pitch b_τ as the period. Then, by means of Fourier decomposition, the following expression can be obtained:

$$\lambda(x) = \frac{a_0}{2} + \sum_{n=1}^{\infty} a_n \cos(\frac{2n\pi}{b_\tau}x), \tag{20}$$

where

$$a_0 = 2 - 2.61859\frac{b_0}{b_\tau}\beta, \tag{21}$$

$$a_n = \frac{0.63662\sin(n\pi) - 0.63662\beta\sin\left(\frac{0.8\pi n b_0}{b_\tau}\right) + \frac{0.397887\beta n b_\tau \cos\left(\frac{0.8\pi n b_0}{b_\tau}\right) b_0}{(nb_0)^2 - 0.390625 \cdot {b_\tau}^2}}{n}, \quad (22)$$

The waveform of air gap magnetic permeance changing with distance is shown in Figure 9.

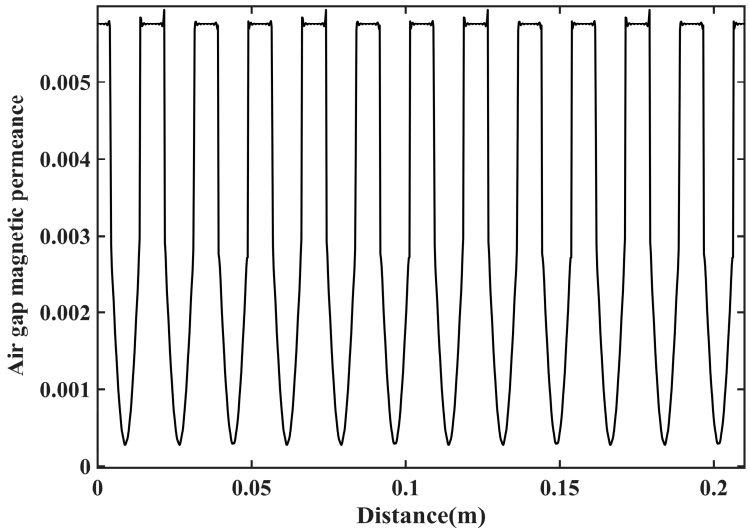


Figure 9. Air gap magnetic permeance varying with distance.

The structure of the LPST is similar to that of a linear motor, and the core is discontinuous. At the breaking point, the end-face magnetic flux will form a closed loop through the primary and secondary side cores and air gaps. Thus, an additional magnetic field is formed in the air gap, as shown in Figure 10. Therefore, the air gap magnetic field of the LPST is composed of the basic traveling wave magnetic field and the pulsating magnetic field. At the longitudinal edge, the magnetic field path is composed of two iron cores and the air gap. The longitudinal end-face flux will produce a pulsating magnetic field with an amplitude that varies with time but does not change with space in the air gap, resulting in the distortion of the air gap magnetic field. This affects the working performance of the linear phase-shifting transformer.

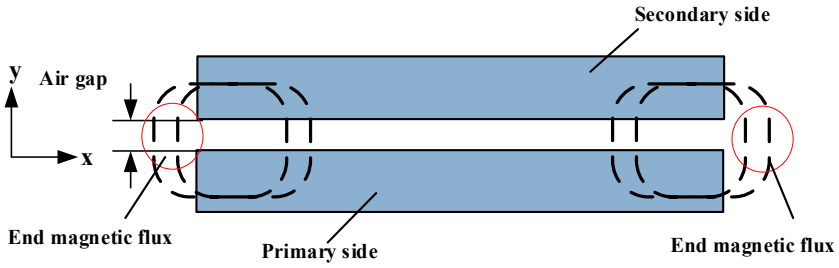


Figure 10. The edge effect diagram of LPST.

It can be seen from Ref. [21] that under the no-load condition, the additional pulsating magnetic field B_{fj} caused by the end effect is expressed as

$$B_{fj} = B_{mz}\cos(\omega t - p\pi), \quad (23)$$

where

$$B_{mz} = -B_\delta \frac{\cos p\pi + \frac{\gamma\tau}{\pi\delta}\sin p\pi}{1 + \gamma\frac{p\tau}{\delta}}, \quad (24)$$

$$B_\delta = \frac{\mu_0 \tau}{\pi\delta} J_1, \quad (25)$$

$$J_1 = \frac{\sqrt{2}m_1\omega K_{w1}I_1}{p\tau}, \tag{26}$$

In the formula, B_{mz} represents the amplitude of the pulsating magnetic field, B_δ represents the amplitude of the basic traveling wave magnetic field, J_1 represents the amplitude of the traveling wave current layer, and γ is the amplitude constant. Referring to the general value in the linear motor, the value of γ is 0.73 in the LPST and m_1 is the number of winding phases.

In summary, the instantaneous value expression of air gap flux density is

$$\begin{aligned} B(x,t) &= f(x,t)\Lambda(x) + B_{fj} \\ &= \left[\sum_{n=1,24m\pm1,\cdots}^{\infty} F_n \sin(n\omega t - \tfrac{\pi}{\tau}x) + \sum_{\nu=6k\pm1}^{\infty}\sum_{n}^{\infty} F_\nu \sin\left(n\omega t \pm \nu\cdot\tfrac{\pi}{\tau}x\right)\right]\cdot \\ &\left[\tfrac{\mu_0}{\delta K_c}\lambda(x)\right] + B_{mz}\cos(\omega t - \pi) \end{aligned}, \tag{27}$$

The radial electromagnetic force of the LPST acts on the surface of the air gap side of the iron core. According to the Maxwell tensor method, its amplitude is proportional to the square of the air gap magnetic flux density $B(x,t)$. The radial electromagnetic force distribution is consistent with the air gap magnetic flux density. Since the air permeability is much lower than the permeability of the ferromagnetic material, the magnetic flux is approximately perpendicular to the primary and secondary side cores. Therefore, the radial electromagnetic force acting on the core can be approximately expressed as [12]:

$$p(x,t) = \frac{B^2(x,t)}{2\mu_0}, \tag{28}$$

where $p(x,t)$ is air gap radial electromagnetic force and μ_0 is air permeability.

4. Finite Element Analysis of Electromagnetic Vibration and Noise of LPST

At present, finite element simulation is a common method to study the vibration and noise of motors and transformers [22–25]. The electromagnetic field analysis of the LPST is realized on the ANSYS Maxwell 2022R1 platform, and the calculations for mechanical vibration and sound field are realized on the ANSYS Workbench 2022R1 platform. The steps of the electromagnetic structure and sound field joint analysis are shown in Figure 11.

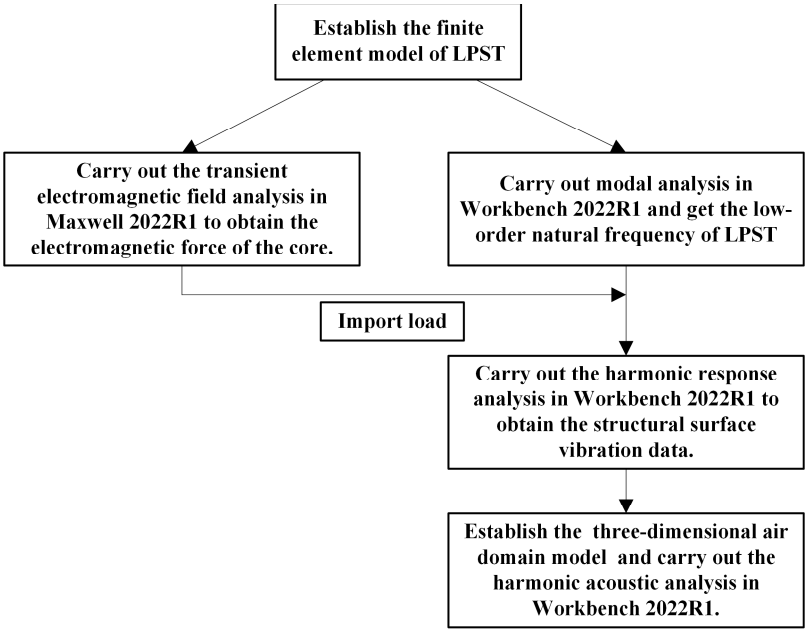


Figure 11. Flow chart of LPST joint simulation.

4.1. Finite Element Simulation of Transient Electromagnetic Field of LPST

To build a two-dimensional model of the LPST in the ANSYS Maxwell 2022R1 software, the first step is to draw the cross-section of the LPST and set the material properties of each part, as shown in Figure 12. The core part selects the silicon steel material of the model 'DW465_50', and the winding part selects 'Copper' in the material library. The second step is to set the boundary conditions. In order to save computing resources and costs, a suitable infinite boundary condition, namely the balloon boundary, is added to the model. The balloon boundary condition is an infinite boundary condition in which the magnetic field can pass through the boundary. The magnetic field under the balloon boundary condition is relatively open, and the solution results of the balloon boundary condition under the same area size are closer to the actual situation than other conditions. Usually, the region of the balloon boundary is a little bigger than the LPST; this is enough for the FEM calculation.

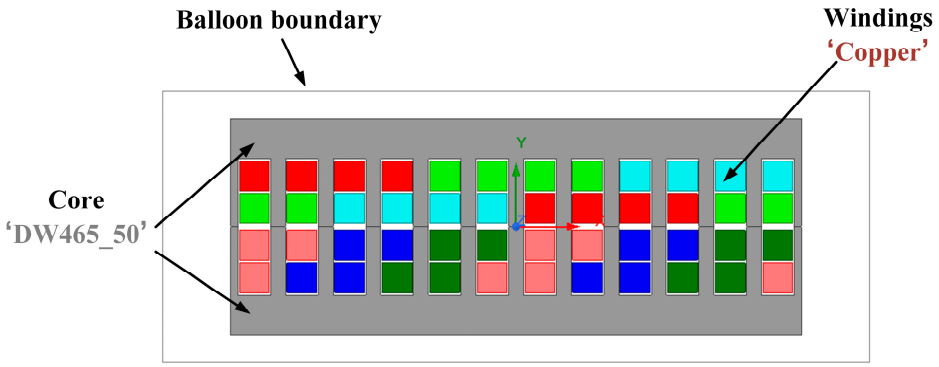


Figure 12. Two-dimensional modal of LPST.

Then, set the excitation source. Here, the external circuit is selected, as shown in Figure 13.

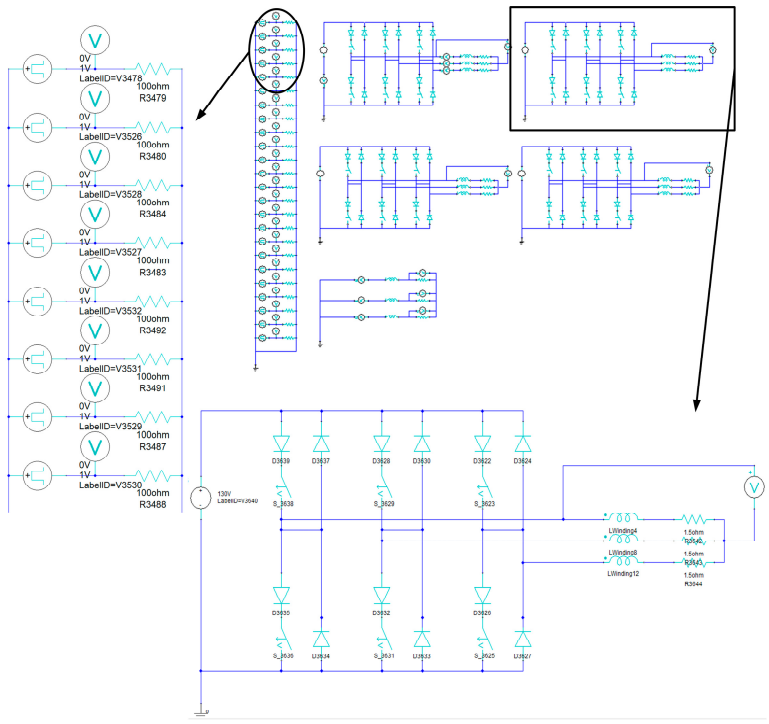


Figure 13. The external circuit of LPST.

Finally, add 'setup' in the 'Analysis' column to set the simulation time and step size and run the entire simulation model. The magnetic field distribution of LPST at t = 0.0011 s in the transient electromagnetic field simulation is shown in Figure 14. The red region indicates that the magnetic density in this region is between 1.8 T and 1.9 T. It shows that the magnetic flux intensity here is higher than in other parts. This is because the magnetomotive force generated by the windings near the region is relatively large at this time. The red area is generally the magnetic saturation area, which mostly appears at the root of the core tooth and the slot opening. The two outermost teeth of the core are thinner than the middle teeth, where the magnetic lines of force are denser and the magnetic flux density is higher. The space–time distribution of the radial electromagnetic force at the air gap of the LPST under no-load conditions can also be obtained, as shown in Figure 15.

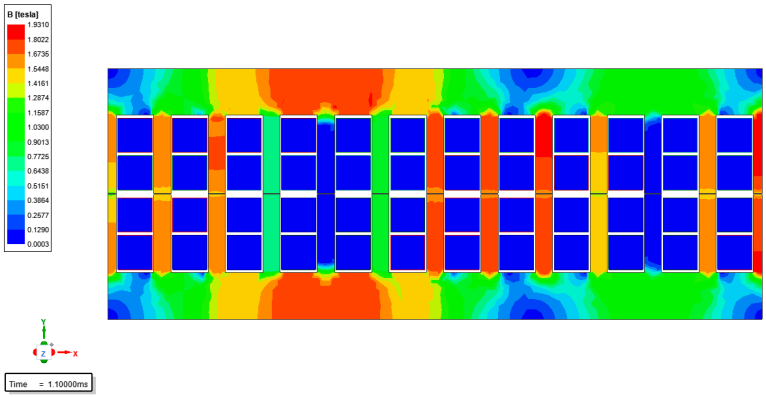


Figure 14. Two-dimensional distribution of LPST magnetic field.

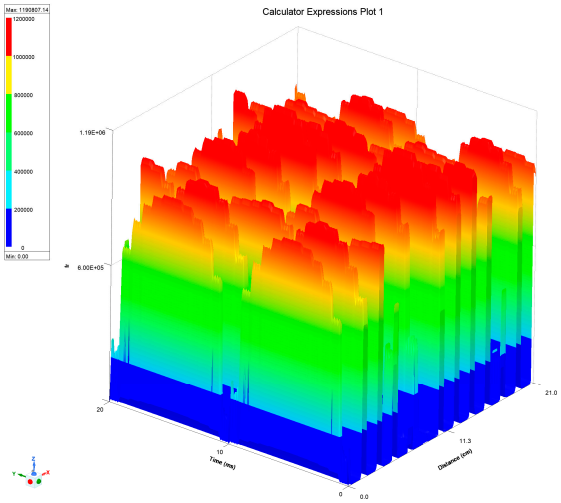


Figure 15. Space–time distribution of air gap radial electromagnetic force (N/m^2).

Taking a point (x = 0.105 m) at the air gap of the LPST, the radial electromagnetic force wave at this point can be solved. Two kinds of time-varying radial electromagnetic force waves obtained by the analytical method and finite element method are shown in Figure 16. Comparing the analytical calculation value with the finite element simulation value, the two are basically consistent, which verifies the accuracy of the analytical calculation model. FFT analysis of the LPST radial electromagnetic force wave is carried out, and the frequency spectrum is shown in Figure 17. From the time spectrum of the radial electromagnetic force, it can be seen that the frequency content at 100 Hz (twice the frequency of the power supply) is the highest, and the harmonic content at 1100 Hz, 1300 Hz, 2300 Hz, 2500 Hz, 3500 Hz, and 3700 Hz is also more prominent than the surrounding frequency.

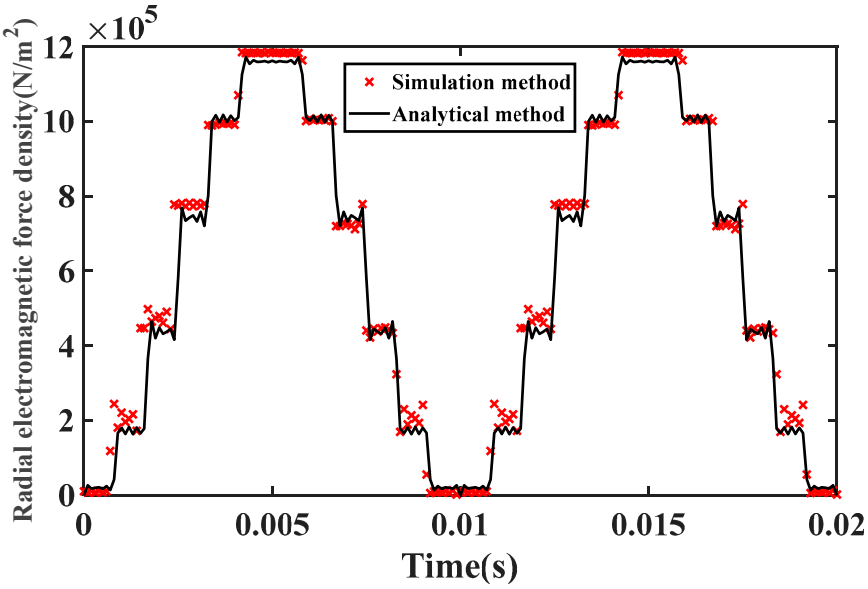


Figure 16. Time distribution of radial electromagnetic force.

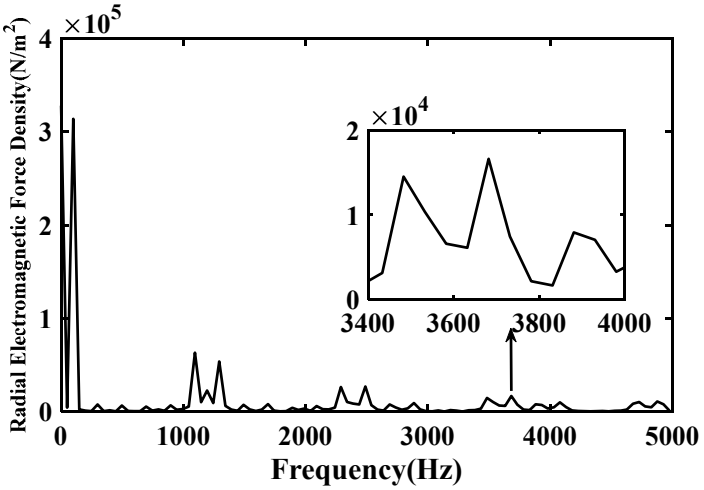


Figure 17. Frequency spectrum of radial electromagnetic force.

4.2. Modal Analysis of LPST

Before the harmonic response analysis, it is also necessary to perform a modal analysis of the LPST and calculate its natural frequency. Firstly, the LPST three-dimensional model is established in ANSYS Workbench 2022R1. The structures of the primary and secondary sides of the transformer are symmetrical, and the radial electromagnetic forces are the same. Therefore, when analyzing the electromagnetic vibration and noise, only the primary side of the transformer is selected. The model simplifies the end winding and is modeled in the form of a breaking winding. The constructed model and material properties are shown in Figure 18 and Table 3.

Table 3. Material properties of LPST.

Material Name	Model	Density (kg/m^3)	Young's Modulus (GPa)	Poisson Ratio
Silicon steel	DW465_50	7700	170	0.260
Copper	C10100	8942	126	0.345

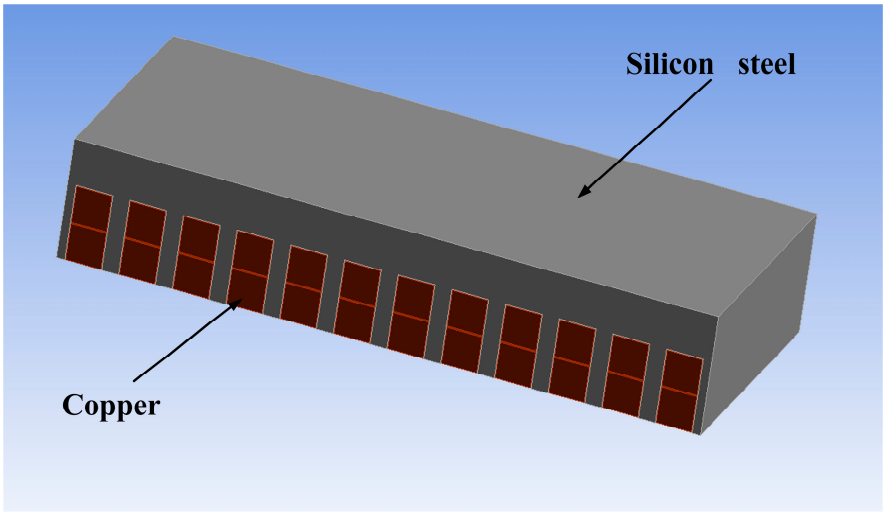


Figure 18. LPST three-dimensional simulation model.

The modal analysis can calculate the natural frequencies corresponding to each mode of the LPST core in the free state, and the first six non-zero natural frequencies are shown in Table 4.

Table 4. The low-order non-zero natural frequency of the LPST in the free state.

Modal Number	Natural Frequency (Hz)
4	98
5	254
6	419
7	3698
8	4419
9	6325

From the modal analysis results of the LPST, as shown in Figure 19, it can be seen that the natural frequencies of 98 Hz, 254 Hz, and 419 Hz correspond to the 0-order mode, and the object undergoes rigid body motion. The frequencies 3698 Hz, 4419 Hz, and 6325 Hz correspond to the first-order mode, of which 4419 Hz corresponds to the torsional mode and 3698 Hz and 6325 Hz correspond to the bending mode.

4.3. Harmonic Response Analysis of LPST

The purpose of the harmonic response analysis is to calculate the response value (usually displacement or acceleration) of the structure in the frequency domain so that the designer can predict the dynamic characteristics of the structure and verify whether the design can overcome the resonance, fatigue, and other harmful effects caused by forced vibration. The basic equation for the harmonic response analysis is

$$\left(-\omega^2 M + i\omega C + K\right)(u_1 + iu_2) = F_1 + iF_2, \tag{29}$$

where ω is the angular frequency of the harmonic excitation, M is the mass matrix, K is the stiffness matrix, C is the damping matrix, u_1 and u_2 are the real and imaginary parts of the vibration displacement, and F_1 and F_2 are the real and imaginary parts of the structural force.

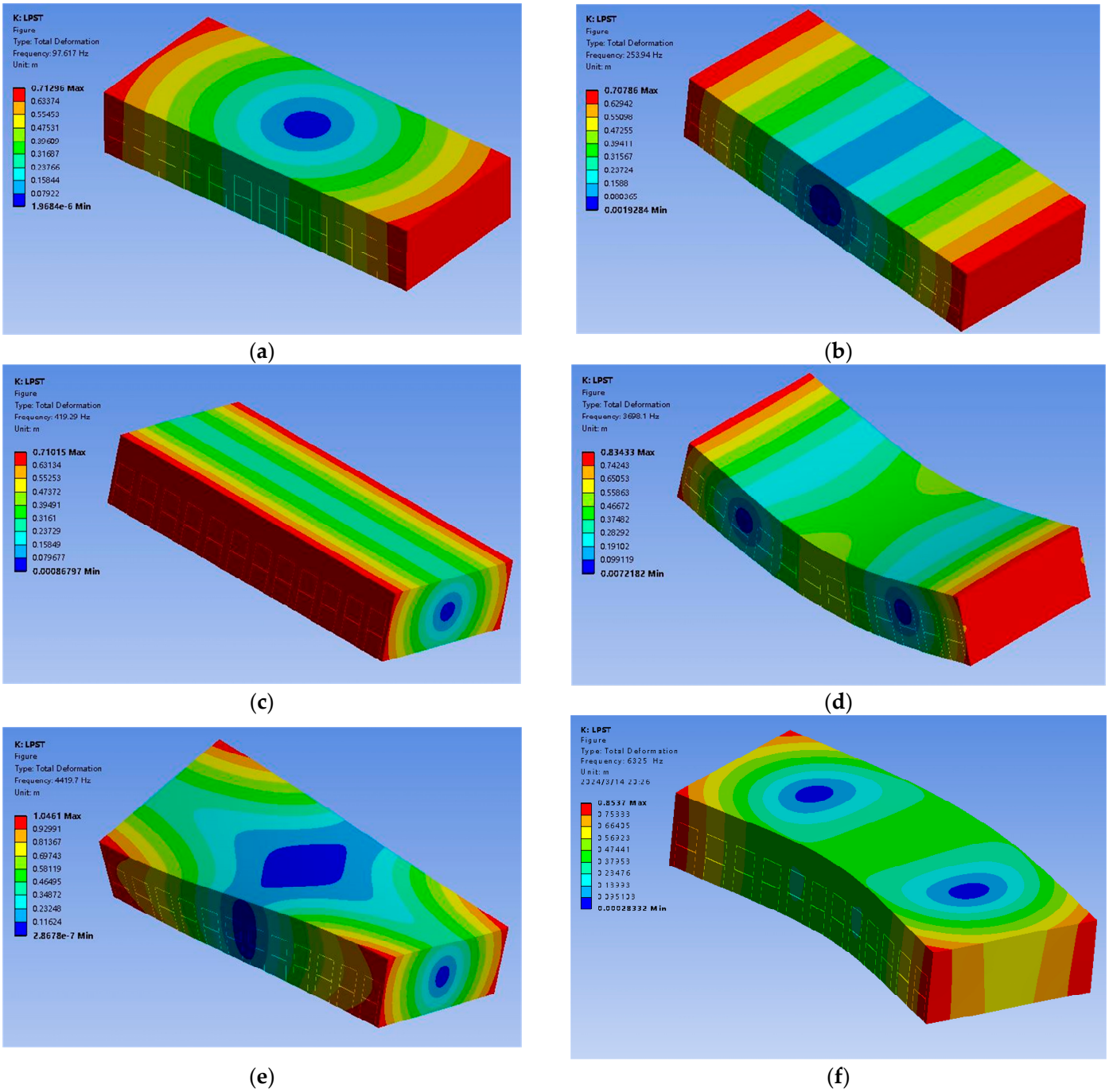


Figure 19. Vibration mode diagram of LPST: (**a**) 98 Hz; (**b**) 254 Hz; (**c**) 419 Hz; (**d**) 3698 Hz; (**e**) 4419 Hz; (**f**) 6325 Hz.

In order to further analyze the influence of the electromagnetic force on transformer vibration during the operation of the LPST, the remote load loading function of the software is used in the ANSYS Workbench 2022R1 platform and the surface force density of the primary structure calculated in the Maxwell 2022R1platform is added to the core tooth surface (the green part in Figure 20) as an excitation source for the coupling analysis.

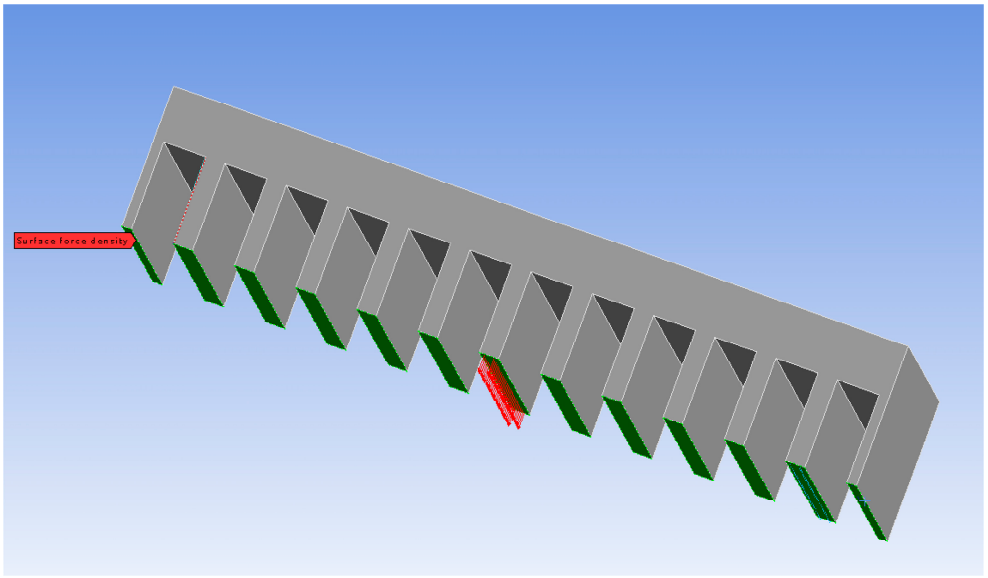


Figure 20. The diagram of load loading.

The electromagnetic force calculated in the electromagnetic field is a force in the time domain which needs to be converted into a force in the frequency domain as the excitation force of the harmonic response. In order to restore the analog signal without distortion, the sampling frequency should be greater than two times the highest frequency in the analog signal spectrum, in accordance with the Shannon sampling theorem. The step size of the finite element analysis in the electromagnetic field is 0.0001 s, that is, the sampling frequency is 10,000 Hz. Therefore, the maximum frequency in the analog signal spectrum should be half the sampling frequency, which is 5000 Hz. The vibration acceleration response spectrum of the primary core surface in the unconstrained state can be solved by the total solution method. The harmonic response analysis results are shown in Figure 21.

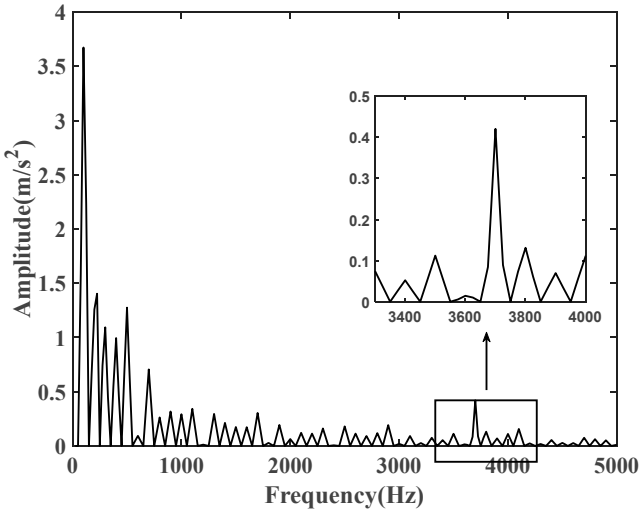
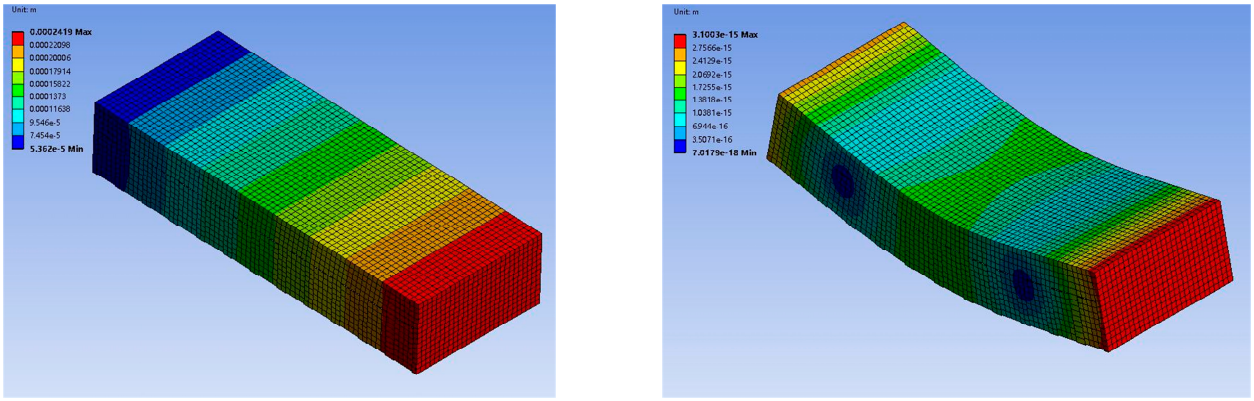


Figure 21. The results of the harmonic response analysis.

The harmonic response results show that the vibration acceleration of the LPST at 100 Hz and 3700 Hz is much larger than the surrounding frequency. The main reason for the obvious vibration at these frequencies is that the components of the radial electromagnetic force wave at the two frequencies are prominent, and the natural frequencies of the 4th and 7th orders of the LPST are 98 Hz and 3698 Hz. When the external excitation frequency is close to the natural frequency of the system, this will cause resonance phenomena and

a large vibration acceleration will be generated. It can be seen from the vibration mode diagram shown in Figure 22 that the LPST is a rigid body mode at 100 Hz, without deformation, and only moves radially. At 3700 Hz, it is a first-order mode, and a deformation with one degree of freedom is generated during vibration.



(**a**) (**b**)

Figure 22. Vibration mode diagram of LPST: (**a**) 100 Hz; (**b**) 3700 Hz.

4.4. Sound Field Analysis of LPST

After completing the harmonic response analysis, the analysis of the sound field is based on pressure acoustics. In the simulation, the boundary vibration acceleration of the LPST structure is coupled to the air domain to solve the sound pressure field in the air domain. The analysis of the LPST noise is based on the harmonic acoustic module in the ANSYS Workbench 2022R1 software. The wave equation is [26]:

$$\frac{1}{\rho c^2}\frac{\partial^2 p_t}{\partial t^2} + \nabla \cdot \left[-\frac{1}{\rho}(\nabla p_t - q_d)\right] = Q_m, \tag{30}$$

where p_t is the total sound pressure, ρ is the fluid density, c is the sound speed, q_d is the dipole sound source, and Q_m is the monopole sound source. In the expression of the wave equation, the speed and density of sound usually depend on space, and only change slowly with time, that is, the sound signal changes slowly on the time scale.

The coupling equation of the structural field and sound field is

$$-\vec{n} \cdot \left[-\frac{1}{\rho}(\nabla p_t - q_d)\right] = -\vec{n} \cdot a_0, \tag{31}$$

$$p_t = p + p_b, \tag{32}$$

where $\vec{n}$ is the unit normal vector from the inside of the acoustic domain to the outside, a_0 is the acceleration of the structural field boundary, p is the static sound pressure, and p_b is the disturbance caused by the sound wave.

The circular air domain with a radius of 1 m is established in the harmonic acoustic module of ANSYS Workbench 2022R1, as shown in Figure 23. It is used to observe the sound pressure distribution of the sound field.

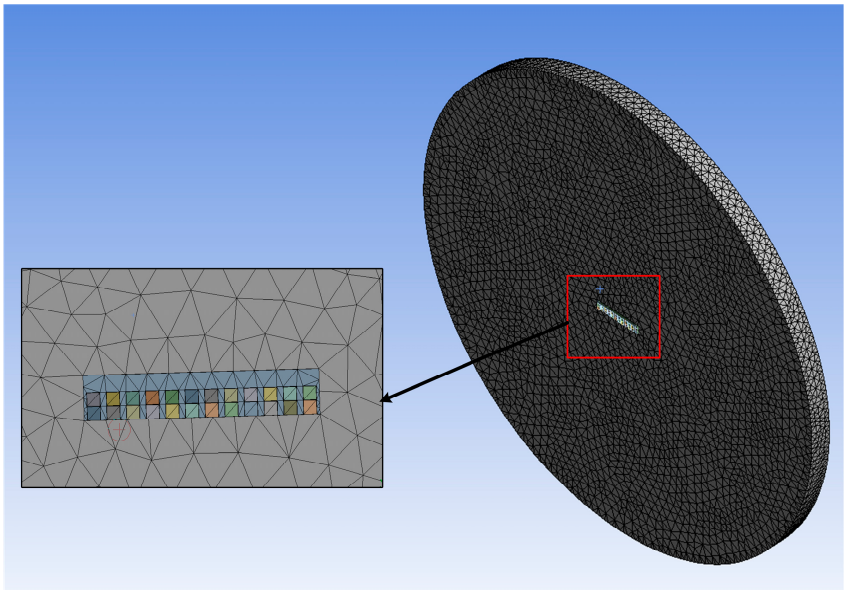


Figure 23. Air domain model.

Through the finite element simulation of the sound field and the calculation of the sound field distribution, the frequency response of the sound pressure level (SPL) at 1 m outside the transformer is obtained, as shown in Figure 24.

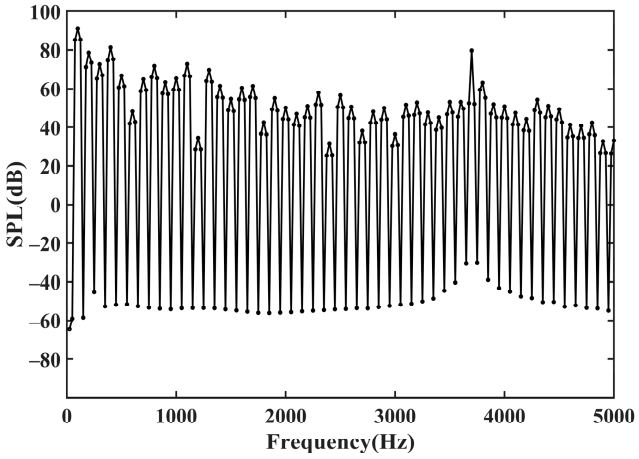


Figure 24. Frequency response of sound pressure level.

In order to simulate the different levels of sensitivity of human hearing at different frequencies so that the objective measurement of sound and the subjective perception of human hearing are approximately consistent, the sound pressure levels of the different frequency components in the sound are usually weighted and corrected. Then, the sound pressure levels of all the frequency components after correction are superimposed to obtain the total sound pressure level of the noise, which is called the weighted sound level. Here, we choose the most commonly used A-weighted sound pressure level (A-SPL) in the noise analysis. Through the finite element solution of the sound field, the A-SPL frequency response at 1 m outside the transformer and the noise distribution in the whole air domain are obtained, as shown in Figures 25 and 26.

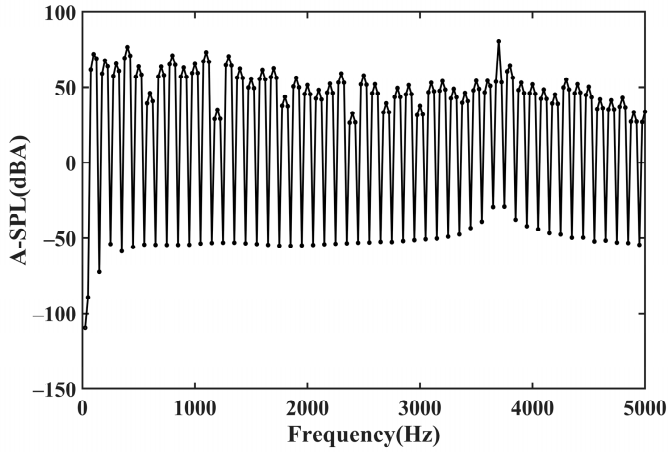
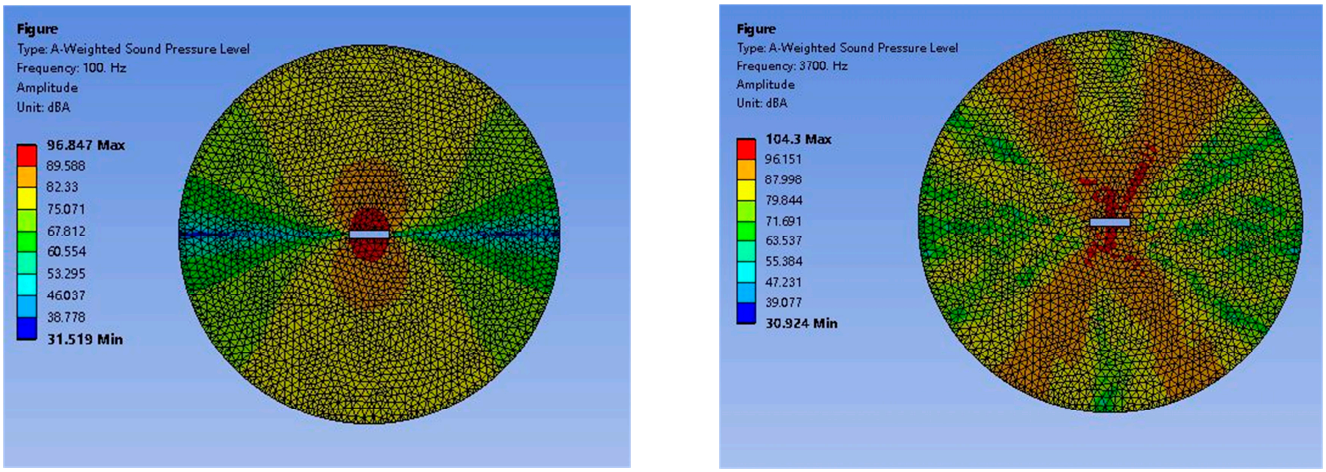


Figure 25. Frequency response of A-weighted sound pressure level.



(**a**) (**b**)

Figure 26. The noise distribution of the LPST: (**a**) 100 Hz; (**b**) 3700 Hz.

The sound field analysis results show that the maximum SPL of the LPST can reach 91.05 dB at a distance of 1 m, and the noise frequency is 100 Hz. At a distance of 1 m, the A-SPL can reach a maximum of 80.75 dBA, and the noise frequency is 3700 Hz. It can be seen that the noise we hear during the operation of the transformer is more likely to be 3700 Hz, which is in the high frequency range. According to the distribution of noise in the range of 1 m, the noise generated by the LPST also radiates mainly along the radial direction.

4.5. The Influence of Fixed Components on the Vibration and Noise of the LPST

In the actual model of the LPST, the core is often wrapped with fixed components. It is usually a structure of insulating material and an external cast iron bracket, as shown in Figure 27. The part in direct contact with the core is PVC insulation material. The contact surface (the lavender-colored part in Figure 28) between the insulating material and the cast iron is set as a fixed support surface in the simulation model, as shown in Figure 26. The natural frequencies of the core under fixed constraint and free conditions are calculated, and the calculated results are shown in Figure 29.

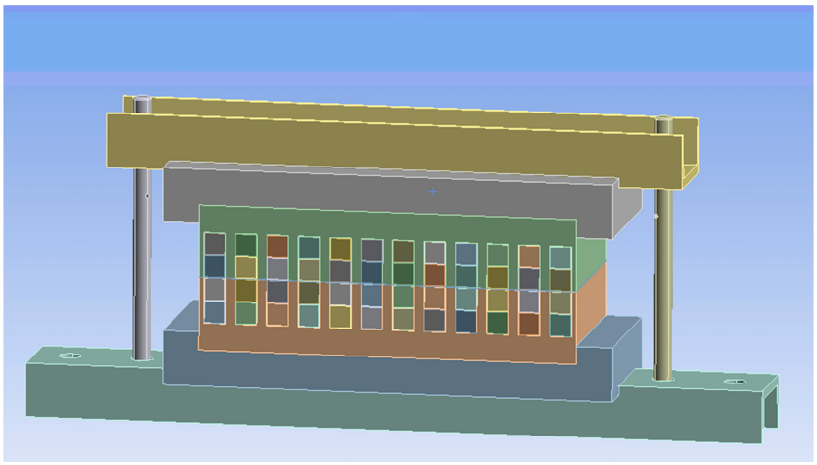


Figure 27. The actual LPST model.

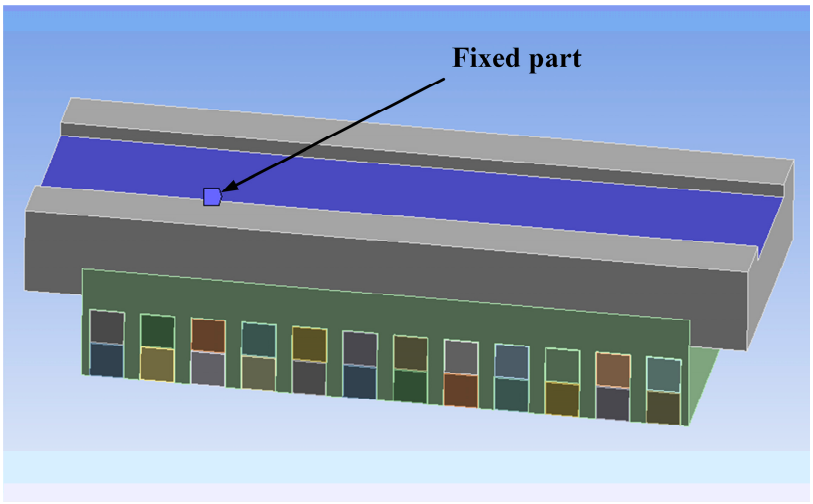


Figure 28. Constrained LPST model.

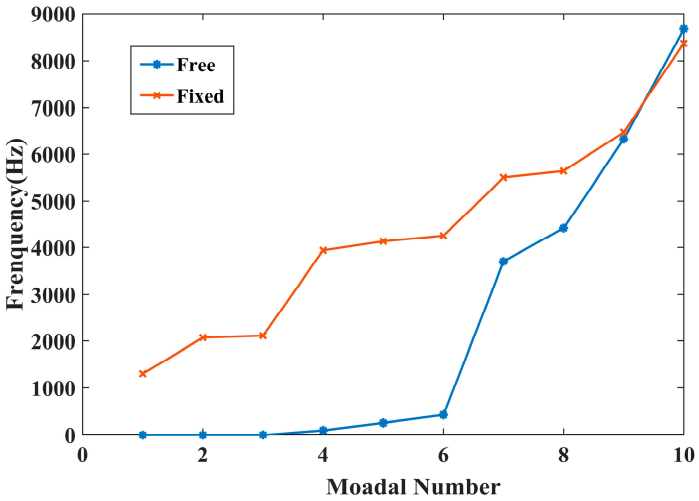


Figure 29. The first 10 natural frequencies in the free and constrained states of the LPST.

It can be seen that in the LPST system with fixed constraints, the natural frequencies of each order are relatively higher than those in the free mode. The natural frequencies of most orders are more than 2000 Hz, which are far from the frequencies with higher radial electromagnetic force content, such as 100 Hz, 1100 Hz, 1200 Hz, 1300 Hz, and so

on. Therefore, the probability of resonance with the radial electromagnetic force is small. Another reason is that the fixed component can limit the displacement of the LPST core to a certain extent, thereby suppressing the size of the resonance. The finite element model of the LPST core under two states is established, respectively, and the electromagnetic vibration and noise results of the core are solved, as the results in Table 5 show. From the comparison of the data in Table 5, it can also be seen that the LPST system with fixed constraints achieves a smaller value, whether in electromagnetic vibration or noise.

Table 5. Vibration and noise data of LPST under different constraint conditions.

Constraint Conditions	Maximum Vibration Response (m/s^2)	Maximum Noise Response (dBA)
Free	3.6725	80.75
Fixed	0.6642	64.864

5. Conclusions

In this paper, the cause of the electromagnetic vibration of the LPST, the radial electromagnetic force wave, was investigated. The influence of the radial electromagnetic force on the electromagnetic vibration and noise of the LPST was explored by theoretical derivation, multi-physical field joint simulation, and comparative verification. The conclusions obtained are as follows:

(1) The expression of the radial electromagnetic force wave was established theoretically, and the spectral and spatial distribution properties of the radial force wave were examined. The accuracy of the statement was then confirmed once more by establishing the LPST finite element simulation model. The maximum frequency of the radial electromagnetic force wave content when the LPST is operating at no load is 100 Hz, which is double the power frequency, and the harmonic content at 1100 Hz, 1300 Hz, 2300 Hz, 2500 Hz, 3500 Hz, 3700 Hz is also more prominent than the surrounding frequency.

(2) The Ansys Workbench 2022R1 platform was used to conduct the joint electromagnetic, mechanical, and acoustic field simulation of the LPST. The response of the LPST's electromagnetic vibration and the distribution of ambient noise were then examined. According to the results, the body will resonate at frequencies of 100 Hz and 3700 Hz due to the radial electromagnetic force of the LPST operating in a no-load state. The high-frequency noise at 3700 Hz, which reaches a maximum of 80.75 dBA, is the primary source of noise that is perceived by the human ear.

(3) The impact of the core's fixed components on its electromagnetic vibration and noise was investigated. According to the finite element modeling results, there is an 82% and 19% reduction in vibration and noise, respectively. These findings demonstrate that core resonance may be successfully avoided and that the magnitude of vibration and noise can be significantly reduced by setting the right limits.

Through the analytical calculation of the radial electromagnetic force of the LPST, we can quickly know which frequency content of the radial electromagnetic force is higher. Resonance creation can be minimized in the LPST design stage by keeping the body's natural frequency away from the frequencies with higher harmonic content. Furthermore, it is feasible to choose the proper fixed support elements to limit the LPST core's vibration. These strategies can be applied to reduce noise and vibration in the LPST, which is the goal of this study and why it is significant. In the next stage, the effects of core mass, shape size, number of fixed points of fixed structure, and pre-tightening force on the vibration and noise of the LPST can also be explored.

Author Contributions: Writing—original draft preparation, D.Y.; writing—review and editing, D.Y. and H.W.; supervision, J.Z. and S.Y.; visualization, D.Y. and C.Z.; software, D.Y. All authors have read and agreed to the published version of the manuscript.

Funding: This research received no external funding.

Data Availability Statement: Data are contained within the article.

Conflicts of Interest: The authors declare no conflicts of interest.

References

1. Zhou, C.; Zhao, J.; Wang, H.; Yan, S.; Yan, D. Harmonic Analysis and Cancellation of Inverter Systems with Linear Phase-Shifting Transformer. *IEEJ Trans. Electr. Electron. Eng.* **2023**, *18*, 1617–1625. [CrossRef]
2. Wang, X.; Li, N.; Yu, T.; Li, T. Study on the Effect of Suspension Windings on the Electromagnetic Vibration and Noise of Ultra-High-Speed Bearingless Permanent Magnet Synchronous Motor for Air Compressor. *IEEJ Trans. Electr. Electron. Eng.* **2023**, *18*, 129–138. [CrossRef]
3. Hou, P.; Ge, B.; Tao, D.; Wang, Y.; Pan, B. Coupling Analysis of Electromagnetic Vibration and Noise of FeCo-Based Permanent-Magnet Synchronous Motor. *Energies* **2022**, *15*, 3888. [CrossRef]
4. Lin, F.; Zuo, S.; Wu, X. Electromagnetic Vibration and Noise Analysis of Permanent Magnet Synchronous Motor with Different Slot-pole Combinations. *IET Electr. Power Appl.* **2016**, *10*, 900–908. [CrossRef]
5. Kim, C.-M.; Choi, M.-I.; Kim, Y.-S.; Bang, S.-B.; Shong, K.-M. Analysis on Characteristics of Core and Winding Vibration in Cast Resin Transformer. *J. Korean Inst. Illum. Electr. Install. Eng.* **2012**, *26*, 52–59. [CrossRef]
6. Zhu, L.; Yang, Q. Research on Vibration and Noise of Power Transformer Cores Including Magnetostriction Effects. *Trans. China Electrotech. Soc.* **2013**, *28*, 1–6+19. (In Chinese) [CrossRef]
7. Hu, J.; Liu, D. Analysis of Transformer Electromagnetic Vibration Noise Based on Finite Element Method. *Trans. China Electrotech. Soc.* **2016**, *31*, 81–88. (In Chinese) [CrossRef]
8. Yang, H.; Chen, Y.; Deng, Z. Electromagnetic Vibration of PM Synchronous Motors with Different Combinations of Slot and Pole Number. *Trans. China Electrotech. Soc.* **2011**, *26*, 24–30. (In Chinese) [CrossRef]
9. Hao, Q.; Hu, Y. Contribution Analysis of Magnetostriction in Motor Electromagnetic Vibration. *Electr. Mach. Control. Appl.* **2011**, *38*, 31–35. (In Chinese) [CrossRef]
10. Li, J.; Cho, Y. Investigation into Reduction of Vibration and Acoustic Noise in Switched Reluctance Motors in Radial Force Excitation and Frame Transfer Function Aspects. *IEEE Trans. Magn.* **2009**, *45*, 4664–4667. [CrossRef]
11. Xiao, Y.; Song, J. The Effect of Harmonics on Electromagnetic Vibration and Noise Characteristic in Inverter-Duty Motor. *Trans. China Electrotech. Soc.* **2021**, *36*, 2607–2615. (In Chinese) [CrossRef]
12. Zhao, M.; Zhao, J. Analysis of Electromagnetic Vibration Characteristics of Transverse Flux Permanent Magnet Linear Motor. *Trans. China Electrotech. Soc.* **2024**, *39*, 168–181. (In Chinese) [CrossRef]
13. Yue, F.; Li, Z. Vibration Mode Calculation and Analysis of U-Type Ironless Linear Motor. *Electr. Appl.* **2018**, 117–122. (In Chinese) [CrossRef]
14. Duan, X.; Zhao, T.; Liu, J.; Zhang, L.; Zou, L. Analysis of Winding Vibration Characteristics of Power Transformers Based on the Finite-Element Method. *Energies* **2018**, *11*, 2404. [CrossRef]
15. Kubiak, W.; Witczak, P. Vibration Analysis of Small Power Transformer. *COMPEL Int. J. Comput. Math. Electr. Electron. Eng.* **2010**, *29*, 1116–1124. [CrossRef]
16. Miao, X.; Jiang, P.; Pang, F.; Tang, Y.; Li, H.; Qu, G.; Li, J. Numerical Analysis and Experimental Research of Vibration and Noise Characteristics of Oil-Immersed Power Transformers. *Appl. Acoust.* **2023**, *203*, 109189. [CrossRef]
17. Javorski, M.; Cepon, G.; Slavic, J.; Boltezar, M. A Generalized Magnetostrictive-Forces Approach to the Computation of the Magnetostriction-Induced Vibration of Laminated Steel Structures. *IEEE Trans. Magn.* **2013**, *49*, 5446–5453. [CrossRef]
18. Jiang, P.; Zhang, Z.; Dong, Z.; Yang, Y. Vibration Measurement and Numerical Modeling Analysis of Transformer Windings and Iron Cores Based on Voltage and Current Harmonics. *Machines* **2022**, *10*, 786. [CrossRef]
19. Liu, Z.; Yang, Z.; Wang, X.; Yu, P.; Li, Z. Design of Multi-phase Permanent Magnet Synchronous Motor with Fractional-slot Windings for Electromagnetic Vibration Reduction Considering Stator Teeth Modulation. *IET Electric Power Appl.* **2023**, *17*, 1123–1135. [CrossRef]
20. Xue, J.; Zhao, J.; Yan, S.; Wang, H.; Zhou, C.; Yan, D.; Chen, H. Modeling and Analysis of New Power Devices Based on Linear Phase-Shifting Transformer. *Processes* **2022**, *10*, 1596. [CrossRef]
21. Zhao, J.; Xu, H. Research on Two Kinds of Longitudinal Side Effects of Linear Phase-Shifting Transformer. *Trans. China Electrotech. Soc.* **2021**, *36*, 984–995. (In Chinese) [CrossRef]
22. Chen, C.; Feng, H. Simulation Analysis of Radiation Noise Characteristics of 220kV Power Transformer. *J. Electr. Power* **2020**, *35*, 515–521. (In Chinese) [CrossRef]
23. Li, R.; Li, C.; Peng, X.; Wei, W. Electromagnetic Vibration Simulation of a 250-MW Large Hydropower Generator with Rotor Eccentricity and Rotor Deformation. *Energies* **2017**, *10*, 2155. [CrossRef]

24. Ling, X.; Tao, J.; Li, B.; Qin, C.; Liu, C. A Multi-Physics Modeling-Based Vibration Prediction Method for Switched Reluctance Motors. *Appl. Sci.* **2019**, *9*, 4544. [CrossRef]
25. Du, J.; Li, Y. Analysis on the Variation Laws of Electromagnetic Force Wave and Vibration Response of Squirrel-Cage Induction Motor under Rotor Eccentricity. *Electronics* **2023**, *12*, 1295. [CrossRef]
26. Liu, Z.; Zhu, L.; Zhong, S.; Wang, Y.; Zhang, J. Active Noise Reduction Analysis and Experimental Research on Electromagnetic Vibration Noise of Transformer. *JAE* **2022**, *70*, 501–513. [CrossRef]

Disclaimer/Publisher's Note: The statements, opinions and data contained in all publications are solely those of the individual author(s) and contributor(s) and not of MDPI and/or the editor(s). MDPI and/or the editor(s) disclaim responsibility for any injury to people or property resulting from any ideas, methods, instructions or products referred to in the content.